TURBULENT DRAG REDUCTION FOR A WALL WITH A BUMP

Jacopo Banchetti & Maurizio Quadrio
Department of Aerospace Sciences and Technologies
Politecnico di Milano, via La Masa 34, 20156 Milano, Italy

INTRODUCTION

This work continues our ongoing efforts to fill the significant gap that still separates skin-friction reduction techniques from industrial applications.

The existing proofs of concept for skin-friction drag reduction are mostly limited to (i) low-Reynolds-number turbulent flows, and (ii) simple geometries, such as flat plates or straight ducts. One naturally wonders whether the established benefits scale up when limitations (i) and (ii) must be overcome, as in industrial applications. Recently, limitation (i) has been shown not to hinder large drag reductions at high Re: on an airplane Gatti & Quadrio [2] estimated that the skin-friction drag reduction achievable at flight Reynolds number by the streamwise-traveling waves (STW) of spanwise velocity, introduced in [5], is at least 23%.

Owing to limitation (ii), though, assessing the overall drag reduction on a body of complex shape, e.g. an airplane, is still a non-obvious task. One could simply surmise that, being the skin-friction component about one half of the whole drag, the potential drag reduction of STW is about 10%. A similar question has been addressed recently in [4], where the effects of riblets on the total aerodynamic drag of an airplane in transonic flight were assessed by RANS. It was found that riblets induce a beneficial change in the pressure distribution around the airplane, leading to an accompanying reduction of pressure drag. A similar work was presented by our group at the last European Drag Reduction and Flow Control Meeting [1], where a model for STW was used in RANS calculation of a transport aircraft: a total drag reduction of about 15% was found instead of the expected 10%.

In the present contribution we employ more reliable prediction tools, and seek answer to the following question: What is the drag reduction produced by skin-friction drag reduction techniques over non-planar walls?

SIMULATIONS

Streamwise-travelling waves (STW) are imposed at the walls of a channel at $Re_b = 3173$. One of the channel walls is non-planar, with a relatively small two-dimensional bump. The DNS solver is the same used in [3]. The non-planar wall is dealt with an implicit immersed-boundary method.

Figure 1 shows a sketch of the computational domain, where one of the channel walls is flat, while the other has a small bump. The domain is composed by two streamwise sections: the upstream section runs a streamwise-periodic simulation, which feeds the downstream one where inflow and outflow conditions are used. The computational domain has dimensions of $(L_x, L_y, L_z) = (24.56h, \pi h, 2h)$ in the streamwise, spanwise and wall-normal directions respectively, being
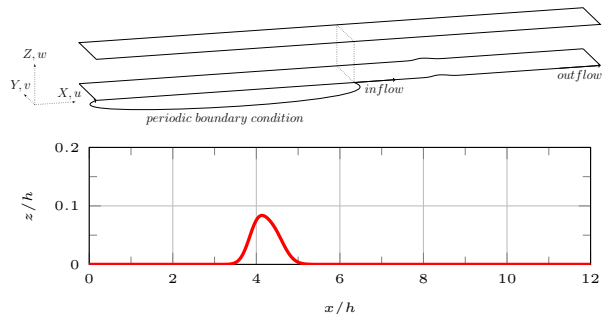

Figure 1: Top: sketch of the computational domain, with the reference system (z is the wall-normal direction). Bottom: bump geometry, of maximum height $0.084h$ (note the enlarged vertical axis).
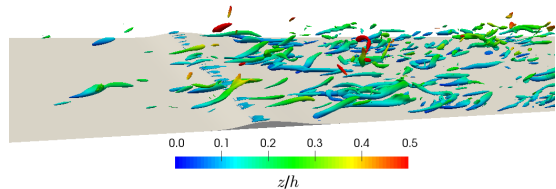

Figure 2: Isosurfaces of λ_2 in an instantaneous flow field, over the bump without STW. Isosurfaces are color-coded with the wall distance.

h the half-width of the channel in the flat sections. About 9×10^7 grid points are used.

Two DNS are carried out, with and without STW. The spanwise wall forcing is specified as:

$$V_w(x,t) = A \sin\left(\kappa_x x - \omega t\right). \tag{1}$$

where V_w is the spanwise velocity at the wall, A is its maximum amplitude, and κ_x and ω represent the spatial and temporal frequencies of the oscillation. The numerical values of the parameters are chosen to guarantee large amounts of skin-friction drag in the plane channel. In outer units, we select $A = 0.75$, $\omega = \pi/10$ and $\kappa_x = 1$. When the forcing is active, it is applied to the precursory simulation too.

RESULTS

To begin with a qualitative picture of the flow (without STW), figure 2 portrays the appearance of turbulent vortical structures over the bump. Isosurfaces of the intermediate eigenvalue λ_2 of the velocity gradient tensor are plotted. Even though the height of the bump is quite small, the localized increase of turbulent activity immediately downstream of the
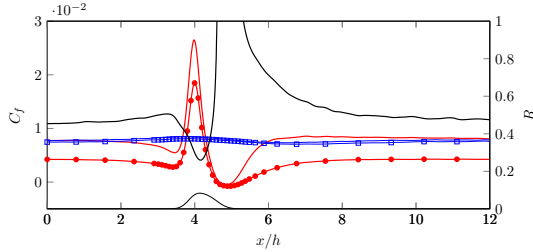
Figure 3: Comparison of $C_f(x)$ between the reference (lines) and the actuated (lines with symbols) case, and local friction reduction rate R (black line, right axis). Red is the bump wall, and blue is the opposite, planar wall. Bump profile is shown at the bottom.

bump can be appreciated.

Drag is ascribed here to two distinct contributions: skin-friction and pressure. Skin-friction drag is quantified via the friction coefficient:

$$C_f(x) = \frac{2\langle \tau_w \rangle}{\rho U_b^2} \qquad (2)$$

where ρ is the fluid density, τ_w is the longitudinal component of the viscous stress evaluated at the wall, and the averaging operator $\langle \cdot \rangle$ implies taking the mean over time and the spanwise direction. The longitudinal variation of C_f is plotted in figure 3, with and without STW. C_f decreases immediately before the bump and then rises quickly to its maximum value close to the bump tip. The maximum is approximately 3 times the value of the flat wall. After the tip, C_f quickly drops towards zero. The bump induces flow separation, hence C_f takes negative values. Owing to the relatively low value of Re, a weak effect of the bump can be observed on the opposite wall, where the distribution of C_f is marginally increased above the bump because of blockage.

With STW applied, $C_f(x)$ remains qualitatively similar, but obviously the friction level are modified by the drag-reduction technique. A local skin-friction reduction rate $R(x)$ is introduced, defined as the relative change of skin-friction coefficient $C_f(x)$ between the controlled and the reference flow:

$$R(x) = 1 - \frac{C_f(x)}{C_{f,0}(x)} \qquad (3)$$

where $C_{f,0}$ refers to the reference case. Way upstream of the bump, R is $\approx 45\%$ which is the expected value for STW in the indefinite plane channel flow at the same Re at these values of the parameters. When the bump is approached, R first increases slightly above 50% immediately upstream of the bump, and then decreases to 25% over its fore part. After the tip, STW are observed to enlarge and intensify the separation bubble. The extrema of the bubble in the unforced case, marked by zero points for $C_{f,0}$, correspond to points where R diverges to infinity. The recovery to the plane-channel value of R is quite slow, and in most of the computational domain downstream of the bump peak R remains above this limit.

Establishing the effect of STW on the pressure distribution is the main goal of the present work. Figure 4 plots the streamwise distribution of the pressure coefficient, defined as:

$$C_p(x) = \frac{2\langle p(x) \rangle - p_0}{\rho U_b^2} \qquad (4)$$

where the reference pressure p_0 is arbitrary in an incompressible flow, and is set to zero at the outlet. To facilitate comparison, in figure 4 the pressure curves have been vertically shifted in such a way that they coincide at $x/h = 0$.
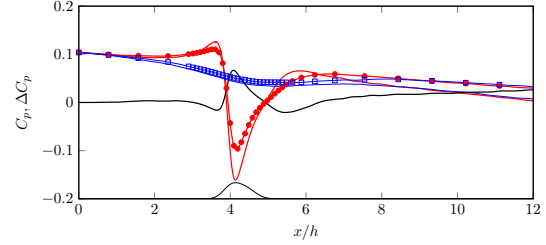

Figure 4: Comparison of $C_p(x)$ (vertically adjusted such that they are coincident at $x/h = 0$) between the reference (lines) and the actuated (lines with symbols) case. Red is the bump wall, and blue is the opposite, planar wall. Thick black line is the difference between pressure coefficients, $\Delta C_p(x) = C_p(x) - C_{p,0}(x)$. Bump profile is shown at the bottom.

In the unactuated cases, pressure increases before the bump, and a pressure minimum is reached at its tip, followed by a recompression. As already commented for C_f, the bump affects, albeit marginally, the pressure coefficient on the opposite planar wall too. $C_p(x)$ presents the linear decrease (uniform pressure gradient) characteristic of the plane channel flow in the inlet and outlet portions of the computational domain, i.e. far enough from the jump.

The effect of STW is non-trivial. At the inlet, where drag is friction-dominated, the negative slope of the $C_p(x)$ line is milder, because of the lower friction drag. Further on, the positive pressure peak before the bump is noticeably reduced, and the pressure drag associated to the anterior part of the bump is consequently expected to be reduced. Also, the pressure minimum near the bump top is decreased by STW, so that the overall pressure jump between the two local maximum and minimum is reduced by around 20%.

Overall, while friction drag reduction presents rather obvious changes wrt the planar case, changes in the pressure distribution, once translated into drag changes by accounting for the geometry of the bump, result in an additional 10% of pressure drag reduction. Qualitative changes are also observed in several turbulent statistics. Hence, the present work motivates further studies of how skin-friction drag reduction contributes to the overall drag changes when applied over complex geometries, and supports the positive results obtained in previous RANS studies of (modelled) skin-friction reduction techniques over the external surface of a transport aircraft.

REFERENCES

[1] A. Gadda, J. Banchetti, G. Romanelli, and M. Quadrio. Drag reduction of a whole-aircraft configuration via spanwise forcing. In *16th EDRFCM, Monteporziocatone*, 2016.

[2] D. Gatti and M. Quadrio. Reynolds-number dependence of turbulent skin-friction drag reduction induced by spanwise forcing. *J. Fluid Mech.*, 802:553–58, 2016.

[3] P. Luchini. Immersed-boundary simulation of turbulent flow past a sinusoidally undulated river bottom. *Eur. J. Mech. B / Fluids*, 55:340–347, 2016.

[4] B. Mele, R. Tognaccini, and P. Catalano. Performance assessment of a transonic wing-body configuration with riblets installed. *J. Aircr.*, 53(1):129–140, 2016.

[5] M. Quadrio, P. Ricco, and C. Viotti. Streamwise-traveling waves of spanwise wall velocity for turbulent drag reduction. *J. Fluid Mech.*, 627:161–178, 2009.